



Extraordinary sensitivity enhancement of Ag-Au alloy nanohole arrays for label-free detection of *Escherichia Coli*

CHARLES SOON HONG HWANG, MYEONG-SU AHN, AND KI-HUN JEONG*

Department of Bio and Brain Engineering, KAIST Institute for Health Science and Technology (KIHST), Korea Advanced Institute of Science and Technology (KAIST), 291 Daehak-ro, Yuseong-gu, Daejeon, 34141, Republic of Korea

*kjeong@kaist.ac.kr

Abstract: Alloy nanostructures unveil extraordinary plasmonic phenomena that supersede the mono-metallic counterparts. Here we report silver-gold (Ag-Au) alloy nanohole arrays (α -NHA) for ultra-sensitive plasmonic label-free detection of *Escherichia Coli* (*E. coli*). Large-area α -NHA were fabricated by using nanoimprint lithography and concurrent thermal evaporation of Ag and Au. The completely miscible Ag-Au alloy exhibits an entirely different dielectric function in the near infra-red wavelength range compared to mono-metallic Ag or Au. The α -NHA demonstrate substantially enhanced refractive index sensitivity of 387 nm/RIU, surpassing those of Ag or Au mono-metallic nanohole arrays by approximately 40%. Moreover, the α -NHA provide highly durable material stability to corrosion and oxidation during over one-month observation. The ultra-sensitive α -NHA allow the label-free detection of *E. coli* in various concentration levels ranging from 10^3 to 10^8 cfu/ml with a calculated limit of detection of 59 cfu/ml. This novel alloy plasmonic material provides a new outlook for widely applicable biosensing and bio-medical applications.

© 2021 Optical Society of America under the terms of the [OSA Open Access Publishing Agreement](#)

1. Introduction

Plasmonic biosensors exploit electromagnetic field localization of noble metal nanostructures for highly sensitive detection of biological samples [1,2]. Target samples near plasmonic substrates typically increase the effective refractive index of surrounding medium, thereby red-shifting the plasmonic resonance wavelength depending on the sample concentration [3–8]. Conventional biochemical detection methods such as enzyme-linked immunosorbent assay (ELISA), polymerase chain reaction (PCR), and flow cytometry require highly experienced technicians for time-consuming pre-treatment labeling procedures at the potential risk of severe sample damage [9]. Such technical bottleneck restricts the utilization of widely applicable biosensing platform for portable point-of-care testing devices. In contrast, the nanofabrication of noble metal plasmonic nanostructures such as metal thin film, nanopillars, nanorods, nanorings, nanodisks, and nanohole arrays actively allows label-free, low-cost and rapid detection of target analytes [10–18]. In particular, plasmonic nanohole arrays (NHA) show surface plasmon induced extraordinary optical transmission from subwavelength apertures and thus have gained exceptional interests as a convenient and efficient biosensing platform [10,19–23]. Unlike classical Kretschmann configurations based on complex prism-coupling optics, plasmonic nanohole biosensors employ compact and linear POC configurations as well as high figure-of-merits, compared to other nanostructures [24]. However, developing highly sensitive plasmonic biosensor still remains a technical issue due to a limited detection volume between the analytes and the resonant sites [25].

Plasmonic resonance wavelength (λ_{PRW}) is mainly determined by the geometric structure (a_0), the dielectric function of plasmonic materials (ϵ_m), and the refractive index of surrounding medium (ϵ_d) [26,27]. The refractive index sensitivity, i.e., a ratio of the shift in the plasmonic resonance wavelength to the change in surrounding index of the medium ($\Delta\lambda_{PRW}/\Delta\epsilon_d$), is therefore also dependent on both the structural design and the dielectric function [28–30]. Previous works have improved the refractive index sensitivity of plasmonic biosensors exclusively through either modifying the geometric parameters such as thickness, periodicity, and diameter or introducing novel three-dimensional nanostructures such as nanocrescents, Lycurgus arrays, nanowells and etc. [28,29,31–33]. In contrast, the pursuit for a better fit plasmonic material for biosensing applications has been relatively neglected, often limited to simply inter-changing the material to another plasmonic metal [34–37]. In recent years, nanocomposites and nanoalloys of two plasmonic metals have acquired much attention due to their unique optical properties [38–45]. For example, aluminum-gold (Al-Au) and silver-gold (Ag-Au) alloy thin-films exhibit completely different dielectric functions in longer wavelength ranges compared to mono-metal thin-films [41,43]. However, such optical features have not yet been utilized for highly sensitive plasmonic biosensing applications. Here we report nanoplasmonic Ag-Au alloy nanohole arrays (α -NHA) for ultra-sensitive plasmonic biosensing platform, showing exceptional sensitivity compared to those of Ag or Au mono-metal counterparts as well as high resistance to corrosion. The α -NHA is further applied for the highly sensitive label-free detection of *Escherichia Coli* (*E. coli*) bacteria at various concentration levels.

2. Results and discussion

2.1. Ag-Au alloy nanohole arrays for highly sensitive detection of *E. Coli*

A schematic illustration of α -NHA for highly sensitive and label-free detection of biological specimen is displayed in Fig. 1(a). The nanoplasmonic alloy biosensor utilizes extraordinary transmission of nanohole arrays, allowing compact and linear optics that simply comprise in the illumination source, plasmonic active substrate, and detector. Furthermore, the α -NHA fabricated by concurrent thermal evaporation simply allows complete miscibility of Ag and Au. The inset graph in Fig. 1(a) shows the calculated relative sensitivity for plasmonic NHA of different material compositions using the finite-difference time-domain (FDTD) method (Release: 2019a r6, Version 8.21.1933). The simulation was performed assuming uniform square lattice hole arrays with 200 nm diameter, 400 nm periodicity, and 60 nm metal thickness on dielectric substrate with refractive index of 1.4. The substrate directly below the nanoholes were etched by 150 nm. The diameter of nanohole arrays were optimized for highest figure-of-merit, which was defined as the ratio of transmittance intensity at plasmonic resonance wavelength and full-width at half-maxima (FWHM) of the spectrum for varying radius of 20 nm to 180 nm. The α -NHA display the highest sensitivity to the bulk change in the surrounding refractive index ranging from 1.33 to 1.4, showing up to 31% higher refractive index sensitivity than Ag and Au mono-metal NHA. The plasmonic sensitivity is improved by the change in the material property, i.e., the dielectric function, under constant geometric structure (a_0). Figure 1(b) compares the measured dielectric functions of Ag (dashed, black), Au (dotted, black), and Ag-Au alloys (solid, red) using spectroscopic ellipsometry in the visible-NIR wavelength range (M2000D RCT, J. A. Woolam). For a clear comparison, the arithmetic average of the two mono-metals is also illustrated as dash-dotted red line. In the visible range, the permittivity value of the Ag-Au alloys is measured between those of two respective mono-metals, which coincide with the arithmetic average value. In contrast, the dielectric function of alloys clearly deviates in the NIR region, well exceeding the boundaries of two mono-metals.

The dielectric functions of five different ratios of Ag-Au alloy are summarized in Fig. 2(a) and Fig. 2(b). Each 200 nm thin film sample was fabricated on an informal cleaned quartz glass substrate using concurrent thermal evaporation of Ag and/or Au of different ratios ranging

from Ag₂₅Au₇₅ to Ag₇₅Au₂₅. During concurrent evaporation, two thermal tungsten boats are simultaneously heated at different rates. Controlling the respective currents on each thermal boat allows precise determination of the final alloy ratio of the concurrently evaporated thin-film. Note that the imaginary permittivity of all Ag-Au alloy ratios deviates from that of mono-metal Ag or Au in the NIR range, whereas it linearly increases proportionally to the alloy ratios in the visible wavelength range. This is also true for the real permittivity. Both the value and the slope of all ratios of Ag-Au alloys begins within the two mono-metals, but deviates as it reaches NIR wavelength regions. Note that the refractive index sensitivity of plasmonic nanostructures are typically correlated with the value and the slope of permittivity [27]. In particular, the permittivities of 50% alloy ratio exhibit the greatest deviation. This phenomenon is explained by the difference in the electronegativity of Ag (1.93) and Au (2.54). Such difference not only reduce the conduction electron mean free path but also increase plasma frequency and damping constant, all of which determine the dielectric function of plasmonic metals [41]. The exceptional dielectric function of the alloys substantially shifts the plasmonic resonance peaks of NHA in the NIR region, enabling higher refractive index sensitivity. The ellipsometry spectroscopy of other plasmonic alloys such as Al-Ag or Al-Au were further performed to obtain the dielectric functions of the respective materials (Fig. 2(c)). Similar fabrication and substrate preparation were used for aluminum-based alloys as for Ag-Au alloys in Fig. 2(a). The permittivity values of all alloys show indications of exemplary plasmonic material, having negative real permittivity and positive imaginary permittivity values. However, the plasmonic quality factor ($-\epsilon_r/\epsilon_i$) calculated in the NIR wavelength range are higher in Ag-Au (7.05) than Ag-Al (1.15) or Au-Al (1.13), strongly demonstrating Ag-Au alloy as efficient material for plasmonic biosensing applications.

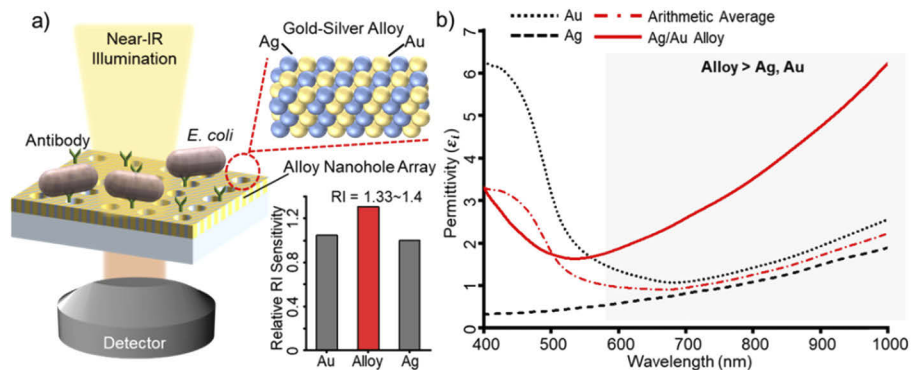


Fig. 1. Ag-Au plasmonic alloy nanohole arrays for highly sensitive and label-free detection of *E. coli*. (a) Schematic illustration of compact and facile detection comprising in alloy plasmonic substrate, detector and illumination. The α -NHA exhibit extraordinary enhancement of refractive index sensitivity than Ag or Au mono-metal NHA. (b) Measured permittivity values for Ag, Au, and Ag-Au alloy. In the NIR region, the dielectric function of Ag-Au alloys significantly deviates from the average value of Ag and Au.

2.2. Nanofabrication of α -NHA

The large-area α -NHA were fabricated using nanoimprint lithography and concurrent thermal evaporation of Ag and Au (Fig. 3). First, NHA with 200 nm diameter and 400 nm period are patterned in square configuration on Si wafer using KrF lithography. Using this as a master stamp, the nanohole pattern is nanoimprinted (Eitre-8, Obducat Co.) onto a 6-inch quartz glass wafer using UV curable polymer (A2 UV-RESIN, EVG Group). Next, hydrophobic anti-stiction layer (1H, 1H, 2H, 2H-Perfluorodecyltriethoxysilane (FDTS), Sigma Aldrich) is treated in a convection oven at 80 °C for 30 minutes to reduce the surface energy. Then, 15 nm thick

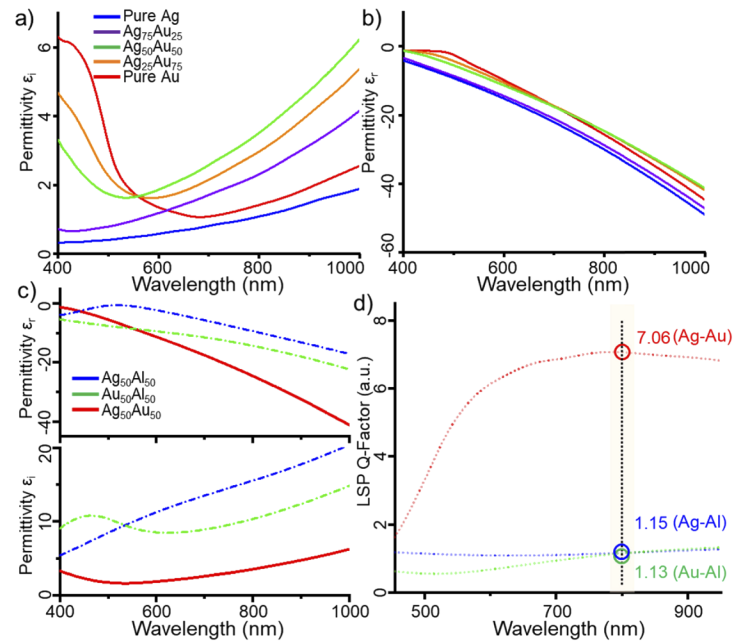


Fig. 2. Real (a) and imaginary (b) permittivities of different ratios of Ag-Au alloys experimentally measured by spectroscopic ellipsometry. (c) Real and imaginary permittivities of Ag-Au, Ag-Al, and Au-Al alloys at 50% alloy ratio. (d) Plasmonic quality factor comparison. The Ag-Au alloys exhibit higher quality factor than aluminum-based alloys in the NIR wavelength region.

Al thin-film is deposited on to the FDTD-treated substrate, followed by concurrent thermal deposition of 60 nm Ag-Au alloy thin-film. The Ag-Au alloy and the aluminum layers are finally pattern-transferred onto a polycarbonate substrate by using an UV-resin (SPC-295, EFiRON Co. Ltd.). The auxiliary UV-resin nano-pillars are completely removed by dry etching, during which the Al film serve as a metal mask. Finally, the aluminum layer is completely removed by dipping in 1% KOH solution for 50 seconds. The KOH solution exhibits extremely selective etch rate for aluminum (> 100 nm/min) compared to Ag or Au (< 1 nm/min). Figure 3(b) shows the scanning electron microscope (SEM) images of successfully pattern transferred α -NHA with high dimensional fidelity. Moreover, the transmittance spectra of α -NHA indicate dramatic blue-shift of the plasmonic resonance wavelengths upon etching of auxiliary nano-pillars and removal of aluminum layer due to the decrease in the effective refractive index (Fig. 3(d)). Figure 3(c) shows the elemental composition analysis of α -NHA measured with energy dispersive spectroscope (EDS-SEM). The EDS-SEM analysis clearly confirms that α -NHA with alloy ratio of $47.4 \pm 0.4\%$ Ag and $52.3 \pm 0.2\%$ Au have been fabricated with complete miscibility of Ag and Au. Figures 3(e) and 3(f) show the reflective and transmissive optical images of the NHA of different compositions on a large area of 64 mm^2 , respectively. The reflection images display a smooth transition of colors demonstrating the pattern uniformity of NHA. In contrast, red, blue, and green colors are explicitly distinguishable in the transmissive optical images, which result from the spectral combinations of main, secondary or tertiary plasmonic resonance peaks.

2.3. Refractive index sensitivity of Ag-Au alloy nanohole arrays

The α -NHA exhibit enhanced refractive index sensitivity as well as material stability. Figure 4(a) shows the normalized transmission spectra of Ag, Ag-Au alloy, and Au NHA in the vis-NIR

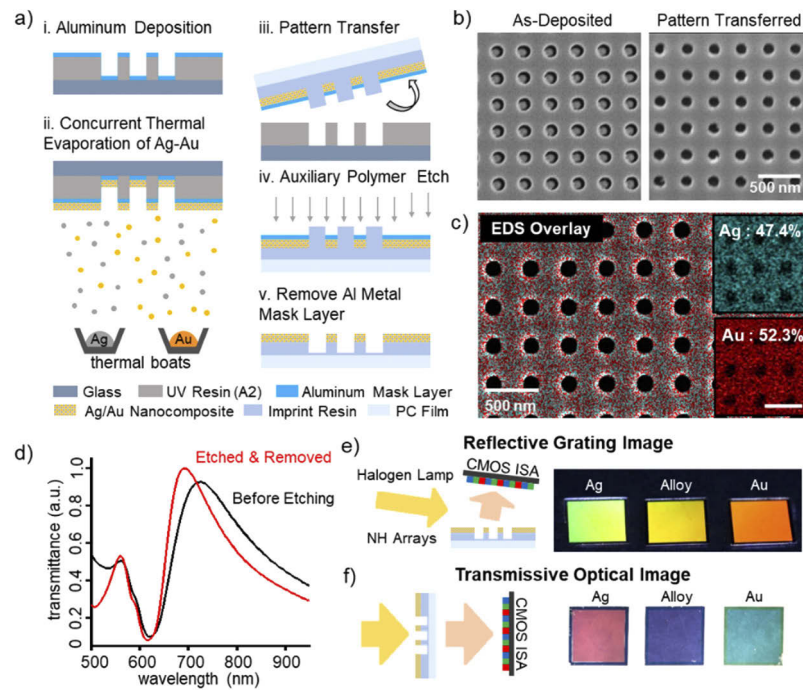


Fig. 3. Large-area nanofabrication of α -NHA. (a) The fabrication process utilizes pattern transfer using nanoimprint lithography and concurrent thermal evaporation. The aluminum metal mask and Ag-Au alloy thin-film are consecutively deposited on the nanohole mold, followed by metal pattern transfer. (b) SEM images of the fabricated nanohole arrays. (c) SEM-EDS composition analysis of α -NHA confirming complete miscibility of Ag and Au. (d) Transmittance spectra of α -NHA upon etching and removal of auxiliary nano-pillars and aluminum layer. (e) Reflective and (f) transmissive optical images of Ag, Au, and Ag-Au NHA on 64 mm² substrate. The reflective image shows gradual shift in colors demonstrating pattern uniformity of NHA, while the transmissive images display colors corresponding to their respective plasmon resonance peaks.

wavelength range. The main plasmon resonance peak wavelengths are observed in the NIR region as expected—667 nm, 691 nm, and 732 nm, respectively for Ag, Ag-Au alloy, and Au NHA. Moreover, the secondary and tertiary plasmonic resonance peaks are observed at 550 nm and 450 nm, respectively. The Ag NHA displays a narrow full-width at half-maximum of transmission spectrum, e.g., 96 nm, however, they often suffer from high susceptibility to surface corrosion. Surface corrosion is particularly detrimental in plasmonic biosensors because the ultra-thin corrosion film on Ag nanostructures significantly reduces the refractive index sensitivity [46]. In contrast, α -NHA show higher material stability than Ag as well as lower FWHM than that of Au. Figure 4(b) experimentally demonstrates strong resistance to surface corrosion in over 40-day period by investigating the plasmonic resonance peak shifts of Ag, Ag-Au alloy, and Au NHA. During the first 15 days, nearly no shift in the resonance peaks are observed for Ag-Au alloys and Au, compared to a dramatic 11 nm red-shift for the Ag NHA. At 40-day mark, the resonance peak of Ag NHA is even further red-shifted by approximately 17 nm while that of α -NHA is shifted by 6 nm, demonstrating superior long-term resistance to surface corrosion. The inset graph in Fig. 4(b) exhibit material stability of α -NHA upon oxygen plasma treatment. The Ag, Ag-Au and Au nanohole arrays were placed in oxygen plasma system under harsh condition of 40 sccm of O₂ and 40 sccm of Ar gas for 30 seconds at 150W plasma power. The α -NHA and the Au NHA

are unaffected by the oxygen plasma system, showing highly distinctive extraordinary optical transmission in the NIR wavelength region. In contrast, the Ag NHA were completely oxidized and shows no discernible plasmonic resonance wavelength.

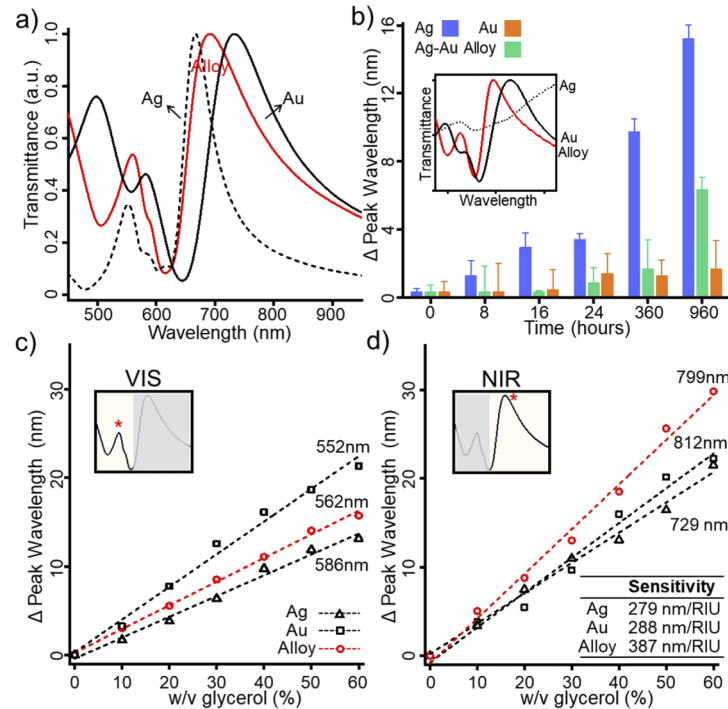


Fig. 4. Refractive index sensitivity and material stability of α -NHA. (a) Transmission spectra of α -NHA compared to mono-metal Ag and Au. The Ag, Au, and α -NHA show plasmonic resonance wave-length at 667 nm, 691 nm, and 732 nm in the NIR region, respectively. (b) Material stability of α -NHA during 40-day period. The plasmonic peak wavelengths of α -NHA remain unshifted, compared to significant red-shift in Ag NHA. Inset shows transmittance spectrum upon oxygen plasma treatment. (c), (d) Refractive index sensitivity of Ag, Au, and α -NHA in the visible (c) and NIR (d) wavelength range. The α -NHA show approximately 40% higher refractive index sensitivity than Ag and Au NHA in the NIR region

Figures 4(c) and 4(d) compares the refractive index sensitivity α -NHA with Ag and Au NHA in both the VIS and NIR wavelength region. The sensitivity was measured by the plasmonic resonance peak shift as the volume-weight concentration of glycerol was increased from 0% to 60% in the glycerol-water mixed solution. As shown in the inset graphs, the peak shift of main and the secondary plasmonic resonance wavelengths were each measured to calculate the sensitivity in the NIR and VIS wavelength range. First, the refractive index sensitivity in the VIS range (Fig. 4(d)) was measured as 253 nm/RIU, 197 nm/RIU, and 164 nm/RIU, respectively, for Ag, Ag-Au alloy, and Au NHA. In this visible wavelength region, the sensitivity of the α -NHA lies between the two mono-metal NHA. However, the measured sensitivities in the NIR region are 279 nm/RIU, 387 nm/RIU, and 288 nm/RIU, respectively, where the α -NHA shows 38% higher sensitivity than those of Ag and Au NHA. This experimental result is in accordance with the spectroscopic ellipsometry data in Fig. 1(b). Since the geometric dimensions of the α -NHA and mono-metal NHA remain constant, the refractive index sensitivity is significantly affected by the dielectric function of materials.

2.4. Label-free detection of *E. Coli* using α -NHA

The α -NHA were further utilized for label-free plasmonic biosensing by detecting *E. coli* bacteria as target analytes. The transmittance spectra upon loading of *E. coli* onto α -NHA were measured using inverted microscope (Carl Zeiss, Axiovert 200M) equipped with spectrometer (Princeton Instruments, MicroSpec 2300i) under NIR illumination (HAL100, Carl Zeiss) (Fig. 5(a)). The *E. coli* concentrations ranging from 1×10^3 to 1×10^8 cfu/ml were prepared from stock concentration

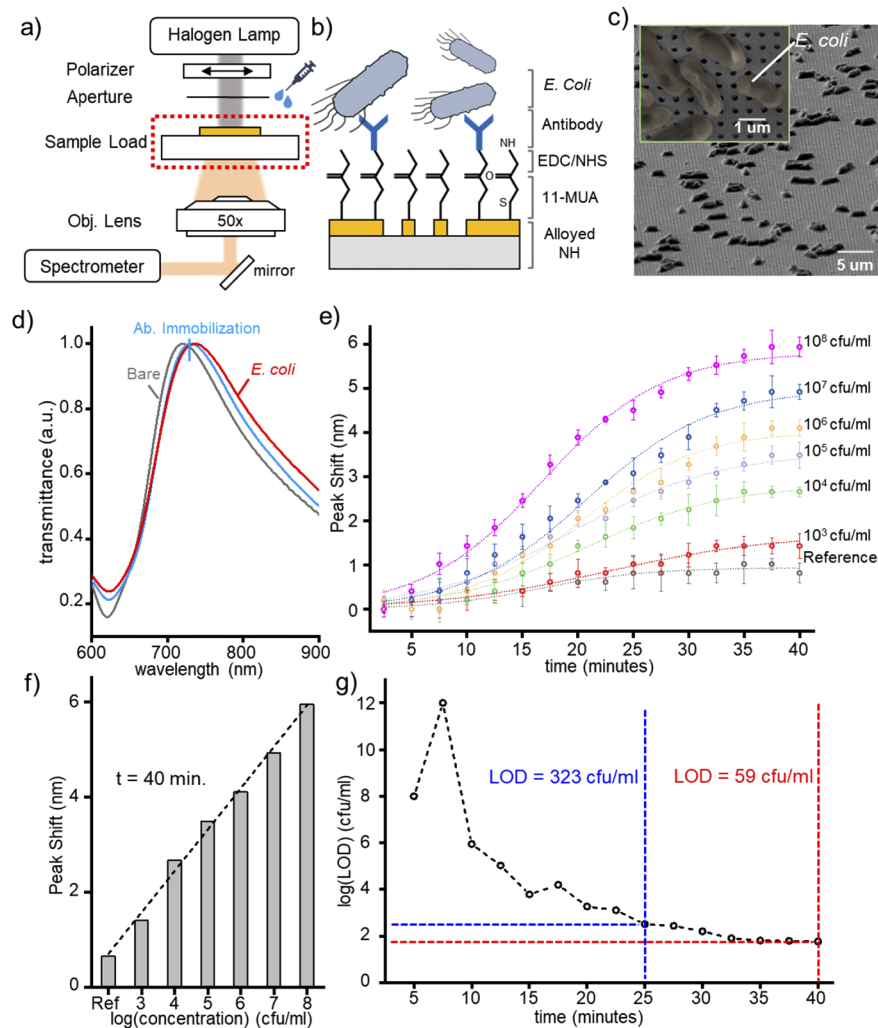


Fig. 5. α -NHA for label-free *E. Coli* detection. Schematic illustration of (a) experimental setup and (b) *E. coli* immobilization. The *E. coli* were covalently bound on the surface of α -NHA through surface modification using EDC/NHS mixtures. (c) SEM image of immobilized *E. coli* on α -NHA. (d) Transmittance spectrum of α -NHA during *E. coli* immobilization process. Each spectrum was measured after rinsing with DI water. The Plasmonic resonance peak is sequentially red-shifted. (e) Time variant measurement of plasmonic resonance peak shifts of α -NHA for various *E. coli* concentration detecting up to 10^3 cfu/ml. (f) Plasmon resonance peak shift for various *E. coli* concentrations at 40 minutes showing a strong logarithmic linear correlation. (g) Calculated LOD of α -NHA during the time-variant measurement.

of 7×10^8 cfu/ml. The initial concentration of bacteria was determined by measuring the optical density of the bacterial solution. Then, each concentration of *E. coli* was covalently bound onto the α -NHA substrate through antibody immobilization (Fig. 5(b)). First, the α -NHA surface was modified in 4 mM 11-MUA (11-Mercaptoundecanoic acid, Sigma-Aldrich) for 8 hours. After sufficient rinsing with ethanol, 40mM-NHS (N-Hydroxy-succinimide, Sigma-Aldrich) / 100mM-EDC (ethyl dimethyl-aminopropyl carbodiimide, Sigma-Aldrich) mixture was treated onto the substrate for one hour. Next, *E. coli* antibody (sc-71004, Santa Cruz Biotechnology) was incubated on the α -NHA for one hour to covalently bond to the NHS/EDC blocks. Finally, the *E. coli* bacteria with concentrations ranging from 10^3 to 10^8 cfu/ml were immobilized onto the α -NHA.

The SEM images in Fig. 5(c) confirm that the *E. coli* are immobilized on the top surface of α -NHA substrate. To further verify the successful antibody immobilization of *E. coli*, the transmittance spectra of α -NHA were measured at each step after rinsing with DI water (Fig. 5(d)). In this experiment, the plasmon resonance peaks are substantially red-shifted in the NIR range by 18 nm after both antibody bonding and *E. coli* immobilization due to higher refractive index of the antibody and *E. coli* than the air [47]. Then, the time variant plasmon resonance peak shift of the α -NHA was measured depending on the *E. coli* concentration ranging from 10^3 to 10^8 cfu/ml (Fig. 5(e)). The transmittance spectra were measured in 150 seconds intervals after the initial introduction of *E. coli*. The *E. coli* were rapidly immobilized onto the substrate in the initial phase and began to saturate after 35 minutes. The α -NHA successfully detected 10^3 cfu/ml *E. coli* by more than 1 nm peak shift, which is a significant improvement from conventional mono-metal plasmonic biosensors that detect 10^4 cfu/ml by less than 1 nm shift [21,48]. Figure 5(f) summarizes the plasmon resonance peak shift of α -NHA after 40 minutes of *E. coli* introduction of different concentrations. As the regression line suggests, the plasmon peak shifts of α -NHA and the logarithmic *E. coli* concentrations follow a linear correlation. Furthermore, the limit of detection (LOD) of *E. coli* was calculated using the equation $\text{LOD} = 3.3(S_y/S)$, where the S_y is the standard deviation of the response and S is the slope of the regression line (Fig. 5(g)). Like the time-variant measurement peak shift in Fig. 5(e), the LOD also begins with nearly 10^8 cfu/ml. However, this value quickly decreases and reaches 59 cfu/ml as the *E. coli* is immobilized. This LOD is approximately three-fold enhancement from previous reports of label-free *E. coli* detection using mono-metal NHA [23]. Note that the label-free detection of *E. coli* with concentration of 10^3 cfu/ml becomes statistically significant after 25 minutes with LOD of 323 cfu/ml.

3. Conclusion

In summary, this work has successfully demonstrated Ag-Au alloy nanohole arrays for ultra-sensitive plasmonic biosensing applications. The facile nanofabrication utilizing nanoimprint lithography and concurrent thermal evaporation allows large-area pattern transfer with high dimensional fidelity. The plasmonic resonance wavelength shifts measured with UV-NIR spectrometer for various glycerol-water mixtures indicate α -NHA provide higher refractive index sensitivity than Ag or Au NHA in the NIR range. The α -NHA further demonstrate the label-free detection of *E. coli* in concentrations down to 10^3 cfu/ml, with calculated LOD of 59 cfu/ml. Moreover, the *E. coli* concentration of 10^3 cfu/ml is statistically distinguished after 25 minutes. This novel alloy plasmonic material can provide a new outlook for highly sensitive and label-free biomedical or environmental sensing applications.

Funding. National Research Foundation of Korea (2016R1A2B301306115); PiQuant Inc.

Acknowledgments. The manuscript was written through contributions of all authors.

Disclosures. The authors declare no competing financial interests.

References

1. A. J. Haes and R. P. Van Duyne, "A nanoscale optical biosensor: sensitivity and selectivity of an approach based on the localized surface plasmon resonance spectroscopy of triangular silver nanoparticles," *J. Am. Chem. Soc.* **124**(35), 10596–10604 (2002).
2. A. Belushkin, F. Yesilkoy, and H. Altug, "Nanoparticle-enhanced plasmonic biosensor for digital biomarker detection in a microarray," *ACS Nano* **12**(5), 4453–4461 (2018).
3. A. Vazquez-Guardado, S. Barkam, M. Peppler, A. Biswas, W. Dennis, S. Das, S. Seal, and D. Chanda, "Enzyme-free plasmonic biosensor for direct detection of neurotransmitter dopamine from whole blood," *Nano Lett.* **19**(1), 449–454 (2019).
4. K. V. Sreekanth, Y. Alapan, M. ElKabbash, E. Ilker, M. Hinczewski, U. A. Gurkan, A. De Luca, and G. Strangi, "Extreme sensitivity biosensing platform based on hyperbolic metamaterials," *Nat. Mater.* **15**(6), 621–627 (2016).
5. X. Lv, Z. Geng, Y. Su, Z. Fan, S. Wang, W. Fang, and H. Chen, "Label-free exosome detection based on a low-cost plasmonic biosensor array integrated with microfluidics," *Langmuir* **35**(30), 9816–9824 (2019).
6. B. Sepúlveda, P. C. Angelomé, L. M. Lechuga, and L. M. Liz-Marzán, "LSPR-based nanobiosensors," *Nano Today* **4**(3), 244–251 (2009).
7. J. A. Jackman, A. Rahim Ferhan, and N. J. Cho, "Nanoplasmonic sensors for biointerfacial science," *Chem. Soc. Rev.* **46**(12), 3615–3660 (2017).
8. A. G. Brolo, "Plasmonics for future biosensors," *Nat. Photonics* **6**(11), 709–713 (2012).
9. A. A. Yanik, M. Huang, O. Kamohara, A. Artar, T. W. Geisbert, J. H. Connor, and H. Altug, "An optofluidic nanoplasmonic biosensor for direct detection of live viruses from biological media," *Nano Lett.* **10**(12), 4962–4969 (2010).
10. J. Park, H. Im, S. Hong, C. M. Castro, R. Weissleder, and H. Lee, "Analyses of intravesicular exosomal proteins using a nano-plasmonic system," *ACS Photonics* **5**(2), 487–494 (2018).
11. W. Kubo and S. Fujikawa, "Au double nanopillars with nanogap for plasmonic sensor," *Nano Lett.* **11**(1), 8–15 (2011).
12. D. P. Lyvers, J. M. Moon, A. V. Kildishev, V. M. Shalae, and A. Wei, "Gold nanorod arrays as plasmonic cavity resonators," *ACS Nano* **2**(12), 2569–2576 (2008).
13. C. Y. Tsai, S. P. Lu, J. W. Lin, and P. T. Lee, "High sensitivity plasmonic index sensor using slablike gold nanoring arrays," *Appl. Phys. Lett.* **98**(15), 153108 (2011).
14. W. C. Shih, G. M. Santos, F. Zhao, O. Zenasni, and M. M. Arno, "Simultaneous chemical and refractive index sensing in the 1–2.5 μm near-infrared wavelength range on nanoporous gold disks," *Nano Lett.* **16**(7), 4641–4647 (2016).
15. P. Singh, "SPR biosensors: historical perspectives and current challenges," *Sens. Actuators, B* **229**, 110–130 (2016).
16. S. K. Vashist, E. M. Schneider, and J. H. Luong, "Surface plasmon resonance-based immunoassay for human fetuin A," *Analyst* **139**(9), 2237–2242 (2014).
17. Y. J. Oh, M. Kang, M. Park, and K. H. Jeong, "Engineering hot spots on plasmonic nanopillar arrays for SERS: a review," *BioChip J.* **10**(4), 297–309 (2016).
18. N. Tawil, E. Sacher, R. Mandeville, and M. Meunier, "Surface plasmon resonance detection of E. coli and methicillin-resistant S. aureus using bacteriophages," *Biosens. Bioelectron.* **37**(1), 24–29 (2012).
19. K. Xiong, G. Emilsson, and A. B. Dahlin, "Biosensing using plasmonic nanohole arrays with small, homogenous and tunable aperture diameters," *Analyst* **141**(12), 3803–3810 (2016).
20. T. W. Ebbesen, H. J. Lezec, H. F. Ghaemi, T. Thio, and P. A. Wolff, "Extraordinary optical transmission through sub-wavelength hole arrays," *Nature* **391**(6668), 667–669 (1998).
21. J. S. Kee, S. Y. Lim, A. P. Perera, Y. Zhang, and M. K. Park, "Plasmonic nanohole arrays for monitoring growth of bacteria and antibiotic susceptibility test," *Sens. Actuators, B* **182**, 576–583 (2013).
22. M. S. Ahn, T. Chung, and K. H. Jeong, "Structural coloration of transmission light through self-aligned and complementary plasmonic nanostructures," *Nanoscale* **10**(14), 6313–6317 (2018).
23. J. Gomez-Cruz, S. Nair, A. Manjarrez-Hernandez, S. Gavilanes-Parra, G. Ascanio, and C. Escobedo, "Cost-effective flow-through nanohole array-based biosensing platform for the label-free detection of uropathogenic E. coli in real time," *Biosens. Bioelectron.* **106**, 105–110 (2018).
24. Y. Xu, P. Bai, X. Zhou, Y. Akimov, C. E. Png, L. K. Ang, W. Knoll, and L. Wu, "Optical refractive index sensors with plasmonic and photonic structures: promising and inconvenient truth," *Adv. Opt. Mater.* **7**(9), 1801433 (2019).
25. J. N. Anker, W. P. Hall, O. Lyandres, N. C. Shah, J. Zhao, and R. P. Van Duyne, "Biosensing with plasmonic nanosensors," *Nat. Mater.* **7**(6), 442–453 (2008).
26. C. S. H. Hwang, M. S. Ahn, Y. Lee, T. Chung, and K. H. Jeong, "Ag/Au alloyed nanoislands for wafer-level plasmonic color filter arrays," *Sci. Rep.* **9**(1), 9082 (2019).
27. D. Y. Lei, J. Li, A. I. Fernandez-Dominguez, H. C. Ong, and S. A. Maier, "Geometry dependence of surface plasmon polariton lifetimes in nanohole arrays," *ACS Nano* **4**(1), 432–438 (2010).
28. S. Larson, D. Carlson, B. Ai, and Y. Zhao, "The extraordinary optical transmission and sensing properties of Ag/Ti composite nanohole arrays," *Phys. Chem. Chem. Phys.* **21**(7), 3771–3780 (2019).
29. H. Chen, X. Kou, Z. Yang, W. Ni, and J. Wang, "Shape- and size-dependent refractive index sensitivity of gold nanoparticles," *Langmuir* **24**(10), 5233–5237 (2008).

30. M. M. Miller and A. A. Lazarides, "Sensitivity of metal nanoparticle surface plasmon resonance to the dielectric environment," *J. Phys. Chem. B* **109**(46), 21556–21565 (2005).
31. T.-W. Chang, X. Wang, A. Hsiao, Z. Xu, G. Lin, M. R. Gartia, X. Liu, and G. L. Liu, "Bifunctional nano lycurus cup array plasmonic sensor for colorimetric sensing and surface-enhanced Raman spectroscopy," *Adv. Opt. Mater.* **3**(10), 1397–1404 (2015).
32. X. Liu, W. Liu, L. Fang, S. Ye, H. Shen, and B. Yang, "Highly sensitive deep-silver-nanowell arrays (d-AgNWAs) for refractometric sensing," *Nano Res.* **10**(3), 908–921 (2017).
33. R. Bukasov and J. S. Shumaker-Parry, "Highly tunable infrared extinction properties of gold nanocrescents," *Nano Lett.* **7**(5), 1113–1118 (2007).
34. M. Focsan, A. M. Craciun, M. Potara, C. Leordean, A. Vulpoi, D. Maniu, and S. Astilean, "Flexible and tunable 3D Gold nanocups platform as plasmonic biosensor for specific dual LSPR-SERS immuno-detection," *Sci. Rep.* **7**(1), 14240 (2017).
35. E. Shkondin, T. Repán, O. Takayama, and A. V. Lavrinenko, "High aspect ratio titanium nitride trench structures as plasmonic biosensor," *Opt. Mater. Express* **7**(11), 4171–4182 (2017).
36. K. L. Lee, H. Y. Hsu, M. L. You, C. C. Chang, M. Y. Pan, X. Shi, K. Ueno, H. Misawa, and P. K. Wei, "Highly sensitive aluminum-based biosensors using tailorable fano resonances in capped nanostructures," *Sci. Rep.* **7**(1), 44104 (2017).
37. J. Ju, W. Liu, C. M. Perlaki, K. Chen, C. Feng, and Q. Liu, "Sustained and cost effective silver substrate for surface enhanced raman spectroscopy based biosensing," *Sci. Rep.* **7**(1), 6917 (2017).
38. D. Rioux, S. Vallières, S. Besner, P. Muñoz, E. Mazur, and M. Meunier, "An analytic model for the dielectric function of Au, Ag, and their alloys," *Adv. Opt. Mater.* **2**(2), 176–182 (2014).
39. Y. Wu, G. Li, C. Cherqui, N. W. Bigelow, N. Thakkar, D. J. Masiello, J. P. Camden, and P. D. Rack, "Electron energy loss spectroscopy study of the full plasmonic spectrum of self-assembled Au-Ag alloy nanoparticles: unraveling size, composition, and substrate effects," *ACS Photonics* **3**(1), 130–138 (2016).
40. C. Gong and M. S. Leite, "Noble metal alloys for plasmonics," *ACS Photonics* **3**(4), 507–513 (2016).
41. O. Peña-Rodríguez, M. Caro, A. Rivera, J. Olivares, J. M. Perlado, and A. Caro, "Optical properties of Au-Ag alloys: An ellipsometric study," *Opt. Mater. Express* **4**(2), 403–410 (2014).
42. S. Kadkhodazadeh, F. A. A. Nugroho, C. Langhammer, M. Beleggia, and J. B. Wagner, "Optical property–composition correlation in noble metal alloy nanoparticles studied with EELS," *ACS Photonics* **6**(3), 779–786 (2019).
43. R. Collette, Y. Wu, A. Olafsson, J. P. Camden, and P. D. Rack, "Combinatorial thin film sputtering $\text{Au}_x\text{Ag}_{1-x}$ alloys: correlating composition and structure with optical properties," *ACS Comb. Sci.* **20**(11), 633–642 (2018).
44. M. Kang, M. S. Ahn, Y. Lee, and K. H. Jeong, "Bioplasmonic alloyed nanoislands using dewetting of bilayer thin films," *ACS Appl. Mater. Interfaces* **9**(42), 37154–37159 (2017).
45. T. Chung, C. S. H. Hwang, M. S. Ahn, and K. H. Jeong, "Au/Ag bimetallic nanocomposites as a highly sensitive plasmonic material," *Plasmonics* **14**(2), 407–413 (2019).
46. X. Wang, C. Santschi, and O. J. F. Martin, "Strong improvement of long-term chemical and thermal stability of plasmonic silver nanoantennas and films," *Small* **13**, 170044 (2017).
47. P. Y. Liu, L. K. Chin, W. Ser, H. F. Chen, C. M. Hsieh, C. H. Lee, K. B. Sung, T. C. Ayi, P. H. Yap, B. Liedberg, K. Wang, T. Bourouina, and Y. Leprince-Wang, "Cell refractive index for cell biology and disease diagnosis: past, present and future," *Lab Chip* **16**(4), 634–644 (2016).
48. G. M. Hwang, L. Pang, E. H. Mullen, and Y. Fainman, "Plasmonic sensing of biological analytes through nanoholes," *IEEE Sensors J.* **8**(12), 2074–2079 (2008).